

Studies of helium poisoning of a Hamamatsu R5900-00-M16 photomultiplier

R. Ospanov^a, M. Kordosky^a, K. Lang^{a*}, J. Liu^a, T. Osiecki^a, M. Proga^a, and P. Vahle^a

^aThe University of Texas at Austin, Department of Physics C1600, 1 University Station, Austin, TX 78712-0264, USA

E-mail: lang@physics.utexas.edu

ABSTRACT: We report results from studies of the helium poisoning of a 16-anode photomultiplier tube R5900-00-M16 manufactured by Hamamatsu Photonics. A tube was immersed in pure helium for a period of about four months and was periodically monitored using a digital oscilloscope. Our results are based on the analysis of waveforms triggered by the dark noise pulses. Collected data yield evidence of after-pulses due to helium contamination of the tube. The probability of after-pulsing increased linearly with the exposure time to helium but the phototube suffered only a small drop in gain, indicating generally strong resilience to helium poisoning.

KEYWORDS: helium poisoning; photomultipliers; PMT; after-pulsing; multi-anode photomultipliers.

*Corresponding author.

Contents

| | |
|---|-----------|
| 1. Introduction | 1 |
| 2. Experimental setup and data sets | 2 |
| 3. Main results | 4 |
| 3.1 Probability of after-pulsing of the M16 | 5 |
| 3.2 Gains and widths of single pulses | 6 |
| 3.3 Gains and widths of after-pulses | 7 |
| 3.4 Time structure of the M16 after-pulsing | 8 |
| 4. Phenomenological estimates of the helium poisoning of M16 | 9 |
| 4.1 Helium permeation in M16 PMTs | 10 |
| 4.2 Ionization of helium atoms in M16 PMTs | 11 |
| 4.3 Estimate of the probability of M6 after-pulsing | 12 |
| 4.4 Timing of after-pulses | 13 |
| 5. Discussion | 13 |
| 6. Conclusions | 14 |

1. Introduction

We report results from studies of helium poisoning of a 16-anode photomultiplier tube (PMT), model R5900-00-M16 (M16), manufactured by Hamamatsu Photonics. This work was motivated by the need to better evaluate the lifetime of the MINOS Far detector [1, 2, 3] which employed about 1,600 of these PMTs [4].

The MINOS Far detector was in continuous operation since its completion in the Summer of 2003 until Summer 2016 [5]. Initially, the detector recorded cosmic ray data, and since the beginning of 2005, MINOS commenced its beam operations using the NuMI neutrino beam at Fermilab.

The MINOS Far detector [3] was installed in a cavern of the Soudan Underground Laboratory located about 705 m underground. This shielding of 2,070 meter-water-equivalent from cosmic rays results in low muon flux of about 0.5 Hz in the entire 5.4 kton detector. The rates in the M16 PMTs are dominated by natural radioactivity (gammas) interacting in the scintillator and the spontaneous emission of light from wavelength-shifting fibers, as reported earlier [6]. Because of these relatively low rates of about 1-2 kHz per PMT, mainly due to single photoelectron pulses, and stable environmental conditions underground, we had expected a long mean lifetime for the M16 photomultipliers employed by MINOS.

However, a neighboring experimental hall in the Soudan laboratory housed the CDMS-II experiment which searched for cold dark matter and which employed a cryogenic helium system [7]. During routine operations of CDMS-II, the concentration of helium in the MINOS cavern was about 60 ppm, but jumped to about 2000 ppm during initial liquid helium transfers in the CDMS-II hall. This can be compared to the concentration of helium in the earth's atmosphere near the earth's surface which in detail depends on location but generally is at the level of about 5-6 ppm. As it is well established, in addition to high rate or current operations, the principal factors affecting the aging of most of photomultiplier tubes is the helium poisoning (i.e., contamination of the PMT vacuum by helium atoms which can permeate from the atmosphere). Though CDMS-II installed later its own venting system for helium handling, the proximity of large amounts of this gas elevated our concerns regarding the lifetime of the MINOS PMTs and directly inspired the tests reported here.

Performance of a PMT depends, among other factors, on the quality of vacuum inside the tube. Residual molecules or atoms trapped inside a tube may be ionized in collisions with (photo)electrons. Such scatterings decrease the electron energy and the effective collection efficiency of the first dynode of a PMT. Positive ions resulting from these collisions can be accelerated toward the cathode where their impact may lead to secondary electron emission and the onset of an additional and time-correlated dynode amplification chain, observed as after-pulsing. The probability of the ionization of the residual gas depends primarily on the gas density, the electron energy, and the distance which photoelectrons travel between a photocathode and the first dynode, or between the dynodes. These processes, generally, decrease an average PMT gain and increase the noise due to after-pulses.

In our studies, we immersed an M16 PMT in helium for about four months, and periodically monitored the PMT dark noise using a digital oscilloscope. We analyzed the time and amplitude structures of recorded waveforms. Our results include studies of the change of the PMT gain and the after-pulsing probability as a function of the cumulative exposure time to helium.

In sections 2 and 3 we describe the experimental setup and present our main findings. In section 4 we provide simple estimates for probability and timing of after-pulses in M16 PMTs. In section 5 we briefly discuss our results.

2. Experimental setup and data sets

The experimental setup, shown in Figure 1, comprised five main components: an M16 PMT with its custom-designed printed-circuit base, a steel container enclosing the helium and the PMT, a dark box, a digital oscilloscope, and a desktop computer which acquired data from the oscilloscope using LabView [8].

M16 PMT has a compact, almost cubical shape of dimensions $24\text{ mm} \times 24\text{ mm} \times 20\text{ mm}$. Figure 2 shows a close-up photograph of such a PMT with an attached base, which serves as a dynode voltage divider and an anode signals router [4]. The square front window is 0.8mm-thick and made out of borosilicate glass. All other sides of the M16 casing are made of KOVAR, a metal alloy with a small coefficient of thermal expansion [9]. The M16 dynode and anode pins protrude from the back of the tube through insulated epoxy-sealed holes.

For our tests we selected a tube with a low dark noise rate and a high gain of about 2×10^7 , achieved at negative 1000 V, the maximum photocathode potential recommended by the manufacturer. At such a high gain, pulses due to single photoelectrons are easily detected by a digital

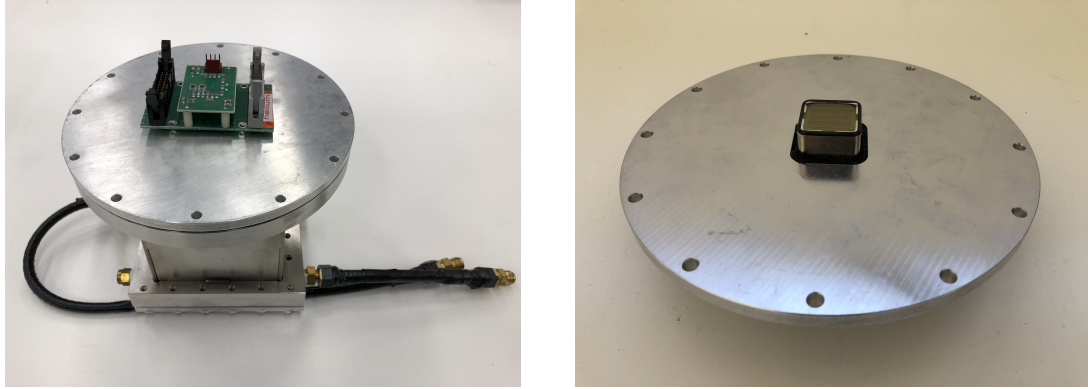


Figure 1. The main part of the experiment – the helium vessel – is shown on the left. The photomultiplier faced helium through a sealed opening in the top flange of vessel.

oscilloscope [10]. The insulated PMT (the KOVAR casing is at the same potential as the photocathode) was installed facing inward and sealed in the lid of a small steel container. The back (i.e., pin)

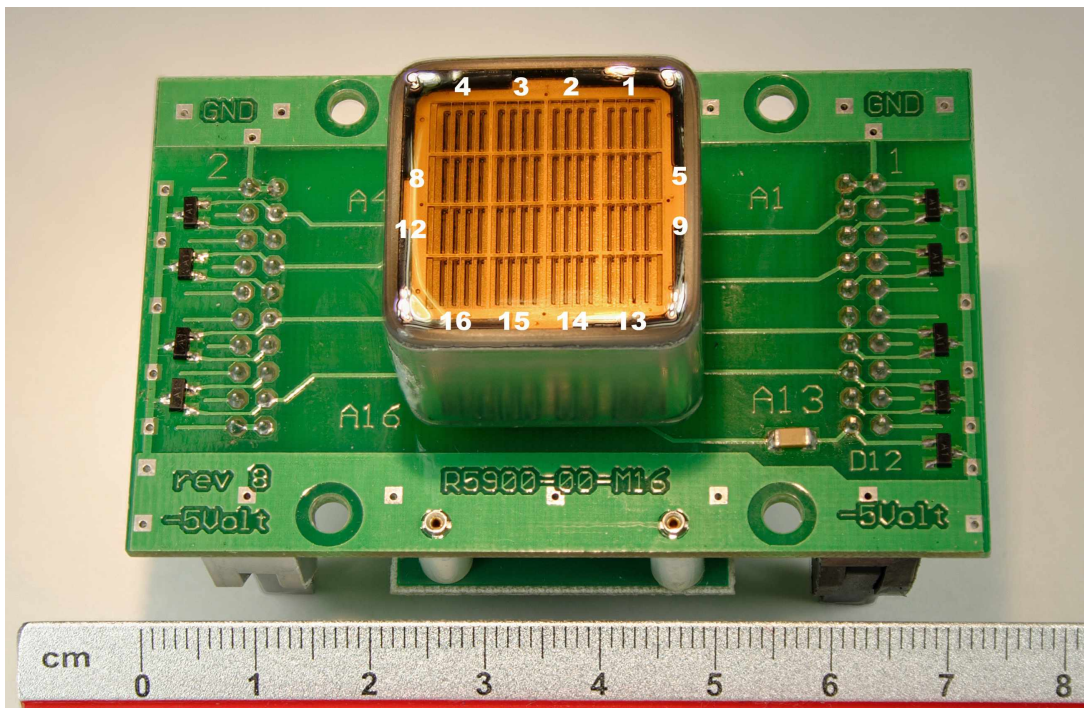


Figure 2. A picture of a M16 PMT with a base. The tube has dimensions of $24\text{ mm} \times 24\text{ mm} \times 20\text{ mm}$ and the casing is made out of a metal alloy called KOVAR. Helium can permeate into the tube primarily through the photocathode window 0.8mm-thick, made out of borosilicate glass and the epoxy sealing pins for dynodes. In the picture we marked pixel numbers in accordance with the factory's numbering scheme which was also used in MINOS.

side of the tube with a mounted base was outside of the helium atmosphere. The steel container had an inlet and an outlet for the helium flow and was placed in a dark box. Special care was taken to assure that all gas and signal connections did not compromise the light-tightness of the dark box. Pure helium was flowed at 10-20 cc/min and resulted in about 100 volume exchanges per day. Due to the gas flow, the pressure of helium in the container was only slightly above the atmospheric pressure.

The compact architecture of the M16 PMT, thus short electron and ion drift distances, led us to expect relatively short (10-100 ns) time separation between dark noise pulses and their helium after-pulses. This guided us to study waveforms triggered by single photoelectrons due to the thermionic (dark) noise from the photocathode. We decided against the use of an external light source since most light sources produce pulses lasting tens of nanoseconds which would obscure or conceal a significant part of the after-pulsing.

We connected individual anodes directly to a digital oscilloscope which was controlled by a specially designed LabView Virtual Instrument application running on MS Windows 2000. The oscilloscope was configured in a self-triggered mode with a threshold set to -12 mV and a maximum sampling rate of 4GS/s. This allowed the readout of waveforms with a 500 ns-wide time window with the trigger time positioned at 20% of the scale (i.e., at 100 ns). It took about 0.2-0.3 s to acquire a single waveform. The internal dead-time of the oscilloscope was about 10 ms. The dark rates of individual anodes varied from 3 to 13Hz.

We conducted the tests over a period of about four months (141 days) in the course of which the tube was continuously immersed in helium. During the first two weeks of the test, the data (individual pixel waveforms) were taken every day. After this initial period, the waveforms were collected once every 10-20 days. The data acquisition took 3-4 hrs per channel.

Each data acquisition session resulted in 80,000 waveforms recorded for pixels 4, 5, 9, 13, and 16 (for some checks we also acquired 150,000 waveforms for pixels 13 and 16). The total number of acquired waveforms was constrained by the acquisition time and available disk space. During our tests, we monitored the high voltage (set to -1000V), and checked the temperature in the laboratory, which stayed constant at $21 \pm 1^\circ\text{C}$, except toward the end of the testing period when the temperature was a couple of degrees lower due to more frequent automatic air-conditioning.

3. Main results

The main objective of the data analysis was to characterize the time and amplitude structure of each acquired waveform. Figure 3 shows four examples of waveforms in our data. A single waveform comprises 2000 time bins spanning 500 ns (i.e., individual bins in a waveform are 250 ps long) with a voltage value for each bin. Each waveform is time and date-stamped. The time resolution of the oscilloscope allowed to resolve near or overlapping pulses, as it is illustrated in the bottom-left panel of Figure 3. The majority of the pulses have a width of about 4-8 ns. A typical waveform with an after-pulse has a second pulse, as shown for example in the top-right panel of Figure 3. We have also observed more complex waveform structures, as shown in the bottom-right panel of Figure 3.

We applied a straightforward procedure to locate and measure characteristics of pulses in each waveform. In our algorithm, a pulse in a waveform was identified by a monotonic voltage change as

a function of bin number denoting time. The time bin with the maximum value of the voltage (i.e., the pulse amplitude) marks the time coordinate (position) of the pulse. At the peak amplitude, the sign of the voltage gradient reverses. Occasionally, the oscilloscope registered waveforms triggered by RF noise. Those were identified as waveforms with a large number of peaks due to sinusoidal RF pulses. We validated the performance of the pulse reconstruction algorithm by visual scanning a significant portion of data.

To minimize the effect of noise, we decided to express the magnitude of the pulse amplitude as the pulse charge, Q , calculated as the area under the pulse: $Q = \frac{1}{R} \int_{t_1}^{t_2} V dt$, where $R = 50 \Omega$. The time-limits of this integral (summation in practice) are defined by points (bins) close to the voltage baseline (ground) for which the pulse amplitude gradient changes sign or becomes zero.

3.1 Probability of after-pulsing of the M16

The probability of after-pulsing was taken as a fraction of waveforms with multiple pulses for each data set, after removing waveforms with the RF noise, as discussed above. In Figure 4 we plot the fraction of waveforms with two pulses as a function of the exposure time to helium. Pixels 4, 13 and 16 in the M16 PMT are all corner pixels. They are slightly larger in area and are more sensitive to a fringe electric field. Pixels 5 and 9 are neighboring edge pixels. Although we observe a clear growth of after-pulsing with time, both the relative and the absolute increase of after-pulsing with time depends on the pixel. These differences between pixels are not well understood. We found no

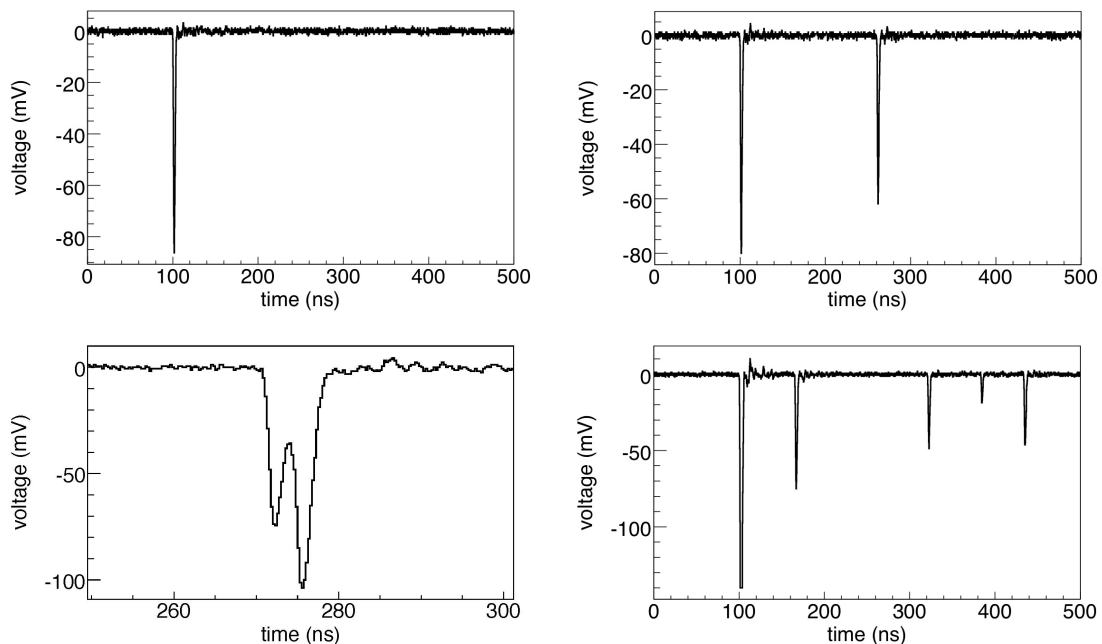


Figure 3. Examples of various waveforms. Top-left: A typical waveform with one peak due to a single photoelectron. Bottom-left: An example of two overlapping single photoelectron pulses (note the difference in the time scale of this plot). Top-right: A typical waveform with an after-pulse. Bottom-right: A rare waveform with five after-pulses ($\ll 1\%$ of all waveforms were of this type).

correlations between dynamic characteristics (like a gain and a dark noise rate) of individual pixels with the trends displayed in Figure 4.

As Figure 4 indicates, the after-pulsing was present at the start of our tests at the level of 2-4% and must be attributed to the initial contamination of the PMT vacuum. The probability of after-pulsing grew with the exposure time to helium. For a corner pixel 4, the increase was about 4%, and for the edge pixels 5 and 9 the increase was about 1% .

3.2 Gains and widths of single pulses

We analyzed the gains and widths of pulses in single-pulse waveforms (i.e., waveforms with no visible after-pulsing). The PMT gain was calculated from the integrated charge of single photoelectron pulses. The gain was examined as a function of the time exposure to helium. The top panel of Figure 5 shows two superposed distributions of the integrated charge for waveforms with a single pulse. The two histograms are for data taken about four months apart (i.e., at the beginning and at the end of our tests). All tested pixels yielded distributions with very similar features, thus, here and in other plots we present results for pixel #4, unless otherwise stated.

The sharp cut-off on the left side of both distributions in Figure 5 reflects the setting of the trigger threshold on the oscilloscope. The left (sharp) peak is due to those photoelectrons which suffered only partial amplification through the dynode chain, typically missing the first dynode, as we identified in our earlier studies [4]. The broad peak, centered around the charge value $Q \approx 3$ pC, is due to a single photoelectron. The position of this peak measures directly the gain of the pixel. The value G of the gain is simply given by $G = Q/e \approx 3 \times 10^{-12}$ [C]/ 1.602×10^{-19} [C] $\approx 1.9 \times 10^7$.

In the bottom panel of Figure 5, we display the mean charge of a single photoelectron pulse as a function of exposure time to helium. The value of each mean was determined by a Gaussian fit performed on each of the 27 data sets collected over the four-month period of our tests. Two examples of such fits are displayed in the top panel of Figure 5. As the data exhibit, the change of gain over the period of four months is small, on the order of 5-10%, and consistent with the expected aging of M16 PMTs [4]. The down trend for the last two data acquisition periods, persistent in

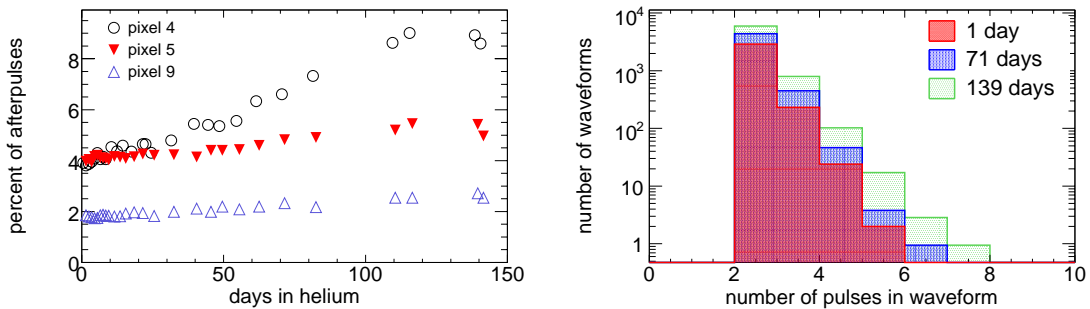


Figure 4. Probability of after-pulsing. Left: A fraction (in percent) of waveforms with two pulses as a function of the exposure time to helium. Right: A distribution of fractions (in percent) of waveforms with more than two pulses. The three superposed distributions were obtained using data taken about two months apart (i.e., at the beginning, in the middle, and at the end of our tests).

several plots, we attribute to the change of temperature in our laboratory which was about 2 – 3°C lower than previously mentioned due to automatic air conditioning which was beyond our control.

Figure 6 shows the widths of the single photoelectron pulses for the waveforms with a single pulse. We use the full-width-at-half-maximum (FWHM), expressed in nanoseconds, as a measure of the width of a pulse. The data show little change over the four-month period of our tests. As indicated above, the last two points were taken at lower laboratory temperature.

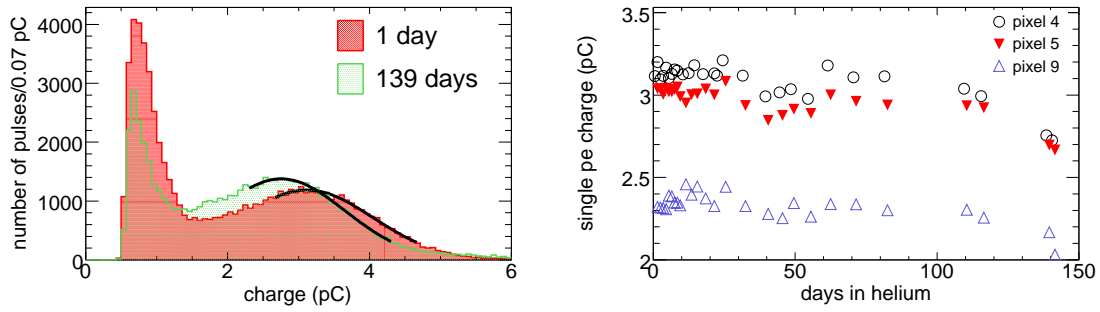


Figure 5. Gain change as a function of the exposure time to helium. Left: Distributions of the integrated charge (in picocoulombs) of a single photoelectron pulse for waveforms with only one pulse (i.e., without after-pulsing). The two histograms are for the data taken about four months apart, at the beginning and at the end of our tests. The position of the peak was initially at 3.12 ± 0.02 pC, and it moved to 2.73 ± 0.02 pC after 139 days in helium. Right: The mean integrated charge of a single photoelectron pulse, determined by fitting histograms as illustrated in the top plot, performed on each of the 27 data sets collected over four months.

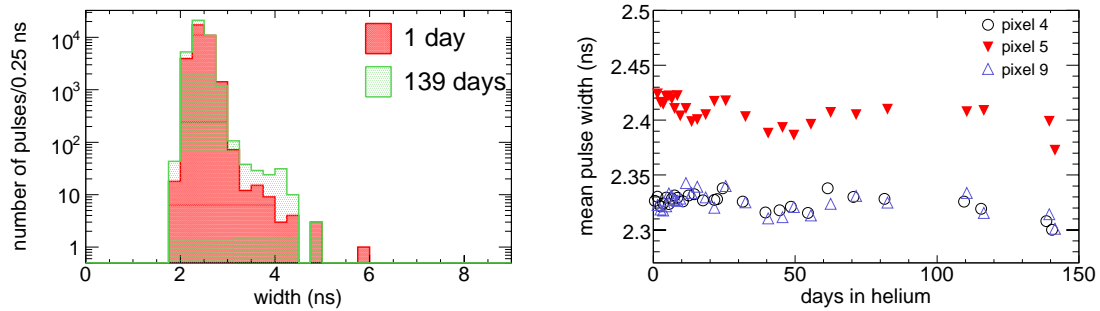


Figure 6. Width change of single photoelectron pulses. Left: A distribution of the FWHM (in nanoseconds) of pulses for waveforms with a single pulse. The histogram is for the data taken at the beginning of our tests and is representative of all the data throughout our tests. Right: The average FWHM of pulses in waveforms with a single pulse as function of the exposure time to helium.

3.3 Gains and widths of after-pulses

The after-pulses were defined as all pulses following the first pulse within the 400ns time window of read out waveforms. Our algorithm was able to clearly identify such waveforms. We first

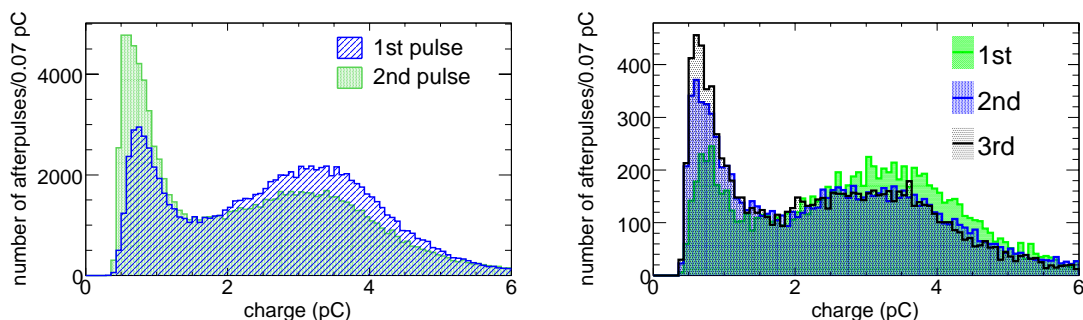


Figure 7. Gains of after-pulses. Left: Superposed distributions of charges of the first and the second pulse for the waveforms with two pulses. The first pulse has a peak at 3.21 ± 0.01 pC and the second is at 3.08 ± 0.01 pC. Right: Superposed distributions of charges of the first, the second, and the third pulse for the waveforms with three pulses. The second pulse has a peak at 3.04 ± 0.03 pC and the third is at 3.02 ± 0.05 pC. These distributions were obtained using all waveforms collected over the entire four-month data-taking period.

examined the gains of pulses for waveforms with exactly two pulses. In the top panel of Figure 7 we compare distributions of the pulse charge for the first (in time) and the second pulse within the 400ns time window. We then compared gains of pulses for waveforms with exactly three pulses. The distributions of the pulse charges for the three pulses are displayed in the bottom panel of Figure 7.

We note that the data clearly indicate that the gains of all pulses (i.e., the gain of the first pulse in a waveform, and the gains of the after-pulses), are very similar and do not change with the exposure time to helium. Figure 8 shows similar comparisons for the pulse widths for waveforms with after-pulses.

We conclude that all pulses in the waveforms with multiple pulses are similar, although the distributions show that the first pulse in such waveforms carries a little more charge than after-pulses, as shown in Figure 8. This may be a result of the complexity of the ionization process of helium (or other residual gases) which occasionally may produce two ionization electrons. In such a rare event, an after-pulse would be preceded by two almost simultaneous electrons initiating a dynode cascade identified as the first pulse.

The mean charge of all pulses is about 3pC (i.e., the gain of about 1.9×10^7) and their average widths (FWHM) remained almost constant during the four-month exposure to helium. The observed variations with time are consistent with the expected aging of M16 PMTs observed previously [4].

3.4 Time structure of the M16 after-pulsing

We then investigated the time structure of waveforms with after-pulses. In the top panel of Figure 9 we display the time separation between pulse 1 and 2 in waveforms with two pulses. The superposed distributions were obtained using three data sets taken two months apart (i.e., at the beginning, in the middle, and at the end of our tests). In the bottom panel of Figure 9 we compare the

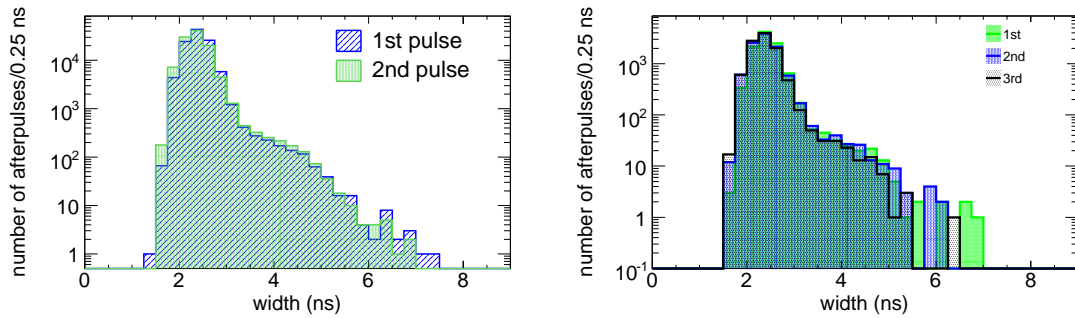


Figure 8. Widths of after-pulses. Left: Superposed distributions of the FWHM for the first and the second pulse for the waveforms with two pulses. Right: Superposed distributions of the FWHM for the first, the second, and the third pulse for the waveforms with three pulses. These distributions were obtained using all waveforms collected over the entire four-month data-taking period.

time separation between pulse 1 and 2 with the time separation between pulse 2 and 3 in waveforms with three pulses. These distributions exhibit similar, although not the same, time characteristics.

The histograms in Figure 9 show after-pulsing time structure with two distinct maxima. As our estimates in section 4 indicate, the first peak, at about 10-70ns, is most likely due to after-pulsing caused by helium ionized between the photocathode and the first dynode. This is because helium ions require about 30ns to accelerate across the distance between the first dynode and the photocathode. The origin of the second broad peak at 150-400ns with a long right shoulder is more speculative. We believe that it is due to after-pulses generated by helium ions produced “deeper” in the dynode channel (i.e., “below” the first dynode) or in the peripheral electric field between dynodes. Some fraction of them may be due to heavier ions. As Figure 9 shows, all these features become more prominent with the increasing exposure time to helium (i.e., the higher helium poisoning of the PMT).

The distributions of the charge carried by the first and the second pulse for pulses separated by either less or more than 100 ns, summarized in Figure 10, tend to support the idea of different location of the helium ionization.

4. Phenomenological estimates of the helium poisoning of M16

In this section we present simple calculations related to the observed after-pulsing due to helium poisoning. Because the exact material properties and the internal dimensions of the M16 PMTs constitute proprietary information, we limit our considerations to “back of the envelope” arguments.

We first estimate the helium permeation rate into the M16 PMT in our setup. We then use the electron-helium ionization cross-section to find the probability for after-pulsing. Finally, we estimate the most probable time of after-pulses due to helium ionization.

Probability of after-pulsing depends on a mean-free-path for ionization by photoelectrons ejected from a photocathode, and the distance and voltage between the photocathode and the first

dynode. For simplicity, the first dynode and the photocathode are treated as infinite conducting parallel plates.

4.1 Helium permeation in M16 PMTs

In our calculations we neglect permeation of helium through the metal walls of the M16. However, helium permeates easily through most glasses due to a small size and high mobility of helium atoms. In the following estimates of the the helium permeation through the front window of the M16 we also ignored the thin layer of photocathode [11].

The rate of permeation depends on the specific glass material, its thickness, the gradient of the helium partial pressure between the two sides of the glass barrier, and the ambient temperature, as given by a steady-state form of Fick's law [12]:

$$\frac{dV}{dt} = \frac{K \cdot A}{D} \cdot \Delta P,$$

where dV is a volume of helium at *STP* which permeates through the surface of area A through a barrier of thickness D in time dt . ΔP is the gradient of the partial pressure of helium and K is the permeation constant which depends on the barrier material.

The value of K for borosilicate glass [13] can be found in two comprehensive compilations [14, 15]:

$$K = 4.8 \times e^{-Q/RT_g} \left[\frac{\text{cm}^3 \cdot \text{mm}}{\text{s} \cdot \text{cm}^2 \cdot (\text{cm Hg})} \right]$$

where for the M16 glass the activation energy $Q = 7,930$ cal/mol, the gas temperature $T_g = 294.15$ K, and the gas constant $R = 1.986$ cal/mol \cdot K. These values give

$$K = 6.1 \times 10^{-13} \left[\frac{\text{cm}^3 \cdot \text{mm}}{\text{s} \cdot \text{cm}^2 \cdot (\text{cm Hg})} \right]$$

For the M16 PMT, $A \approx 5.76$ cm², $D = 0.8$ mm, and $\Delta P \approx 76$ cm Hg, hence $\frac{dV}{dt} = 3.34 \times 10^{-10}$ cm³/s. The volume of permeated helium after one day of exposure to pure helium gas at an atmospheric

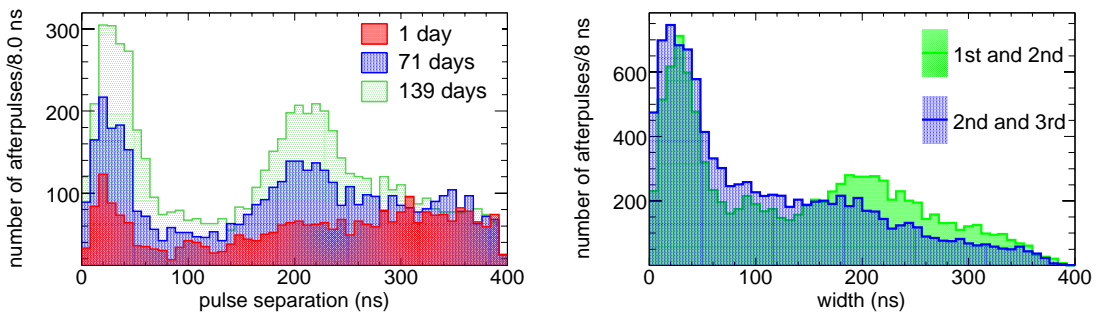


Figure 9. Time separation between pulses. Left: The time period separating two pulses in waveforms with two pulses. The three superposed distributions were obtained using data taken about two months apart (i.e., at the beginning, in the middle, and at the end of our tests). Right: The time separation between pulse 1 and 2, and between pulse 2 and 3, in waveforms with three pulses. These distributions were obtained using all waveforms collected over the entire four-month data-taking period.

pressure ($\Delta P \approx 101 \text{ kPa}$), is: $V_{He}(1 \text{ day}) = 3.34 \times 10^{-10} [\text{cm}^3/\text{s}] \times 24 \times 3600 [\text{s}] \approx 2.88 \times 10^{-5} \text{ cm}^3$. We estimate the gas volume of the M16 tube to be about 10 cm^3 , thus after one day, the partial pressure of helium inside the tube is (at STP):

$$P_{He}(1 \text{ day}) = \frac{V_{He}(1 \text{ day})}{V_{tube}} \times 101 [\text{kPa}] \approx 0.29 \text{ Pa}.$$

This corresponds to $N_{He}(1 \text{ day}) \approx 7.75 \times 10^{14}$ helium atoms penetrating through the glass window of the M16 PMT in one day. Thus, we expect that at the end of our tests, which lasted four months, the number of helium atoms which permeated into the tube to be $N_{He}(120 \text{ days}) \approx 9.3 \times 10^{16}$, which corresponds to the partial helium pressure inside the M16 PMT of $P_{He}(120 \text{ days}) \approx 35 \text{ Pa}$. We will use these results to estimate the effective mean-free-path for helium ionization and the probability of the after-pulsing.

4.2 Ionization of helium atoms in M16 PMTs

The total ionization cross-section of helium atoms depends on the energy of the impacting electron and is well measured for a wide range of energies, as shown in Figure 11 which was reproduced from references [16] and [17]. The cross-section for a single-electron ionization is essentially zero below 25 eV and then grows rapidly reaching a maximum at about 120 eV; it decreases slowly as the energy of an impacting electron increases. The ionization probability is most significant at an energy of about 80-120 eV.

Photoelectrons are accelerated inside the PMT in the electric field between the photocathode and subsequent dynodes. In our tests we used a standard MINOS M16 base with the 12-stage voltage divider which has the photocathode to anode voltage ratios of 2.4-2.4-2.4-1.0-1.0-1.0-1.0-1.0-1.0-1.0-1.2-2.4. The nominal high voltage values in MINOS were set to achieve a gain of about 1×10^6 , which can be reached for most PMTs at 700-900V [4]. In our helium poisoning

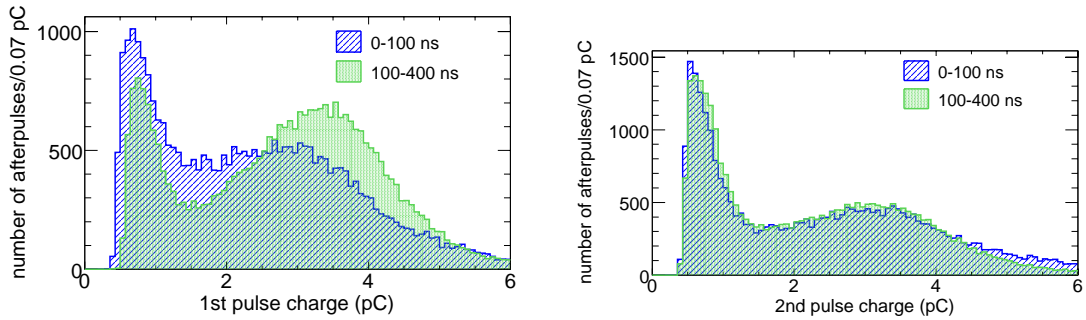


Figure 10. Left: Superposed distributions of the charges in the first peak for waveforms in which the after-pulse is separated from the first (trigger) peak by less than 100ns or separated by time between 100 to 400ns. The first pulse in the 0-100ns pulse category has a peak at $3.29 \pm 0.01 \text{ pC}$ and for the 100 to 400ns category the peak is at $2.72 \pm 0.04 \text{ pC}$. Right: Superposed distributions of the charge in the second pulse for the same pulse categories. The second pulse in the 0-100ns pulse category has a peak at $3.00 \pm 0.02 \text{ pC}$ and for the 100 to 400ns category the peak is at $3.06 \pm 0.01 \text{ pC}$. These distributions were obtained using all waveforms collected over the entire four-month data-taking period.

tests, however, we used the maximum recommended high voltage of 1000 V to maximize the PMT gain, the photoelectron collection efficiency, and the cross-section for helium ionization. For such a setting the voltage difference between the photocathode and the first dynode, ΔV_1 is $\Delta V_1 = \frac{R_1}{R_{total}} \times 1000 \text{ [V]} = \frac{2.4}{17.8} \times 1000 \text{ [V]} = 135 \text{ V}$. We considered changing the voltage divider ratios but decided against it since a modified base would significantly alter operational characteristics of the tube (otherwise extensively studied earlier [4]). A photoelectron is accelerated in the electric field given by $E = \Delta V_1/d$, where $d \approx 1.5 \text{ mm}$ is the distance from the photocathode to the first dynode.¹

The cross-section for ionization grows as the photoelectron gains energy as it approaches the first dynode. The mean-free-path for helium ionization, λ_{He}^{ion} , is given by:

$$\lambda_{He}^{ion} = \frac{1}{n_{He} \cdot \sigma_{He}^{ion}} = \frac{1}{N_{He}/V_{tube} \cdot \sigma_{He}^{ion}},$$

where n_{He} is the density of helium atoms in the tube, and σ_{He}^{ion} is the cross-section for helium ionization. For our estimates we take somewhat arbitrarily $\sigma_{He}^{ion} = 3 \times 10^{-17} \text{ cm}^2$ and the estimated earlier value for N_{He} , after one day in the helium atmosphere we calculate $\lambda_{He}^{ion}(1 \text{ day}) \approx 430 \text{ cm}$, and after the four-month exposure to helium $\lambda_{He}^{ion}(120 \text{ days}) \approx 3.6 \text{ cm}$.

4.3 Estimate of the probability of M6 after-pulsing

Most after-pulsing is caused by positive helium ions drifting to the photocathode, scattering off it, and causing additional photoelectron emission. Thus, the density of helium ions is closely coupled to the probability of after-pulsing. The ionization probability of helium atoms inside M16 is

¹The exact value of this distance is not known to us since this is proprietary information. Here, we provide our best estimate.

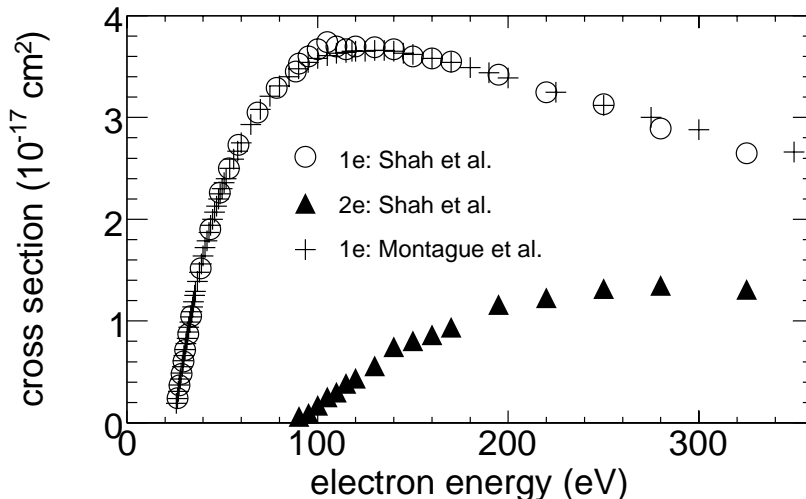


Figure 11. The total ionization cross-section of a helium atom by electrons as a function of the electron energy. The plot is reproduced from [16] (triangles) and from [17] (circles). The two distinct sets of data are for a single-electron ionization (higher set of points) and a double-electron ionization (lower set of points).

proportional to the ratio of the electron path-length between the photocathode and the first dynode to the mean-free-path for helium ionization, λ_{He}^{ion} . The sharp rise of σ_{He}^{ion} with energy means that the ionization process is more likely to occur *near* the first dynode, where photoelectrons are sufficiently energetic. We can *crudely* estimate the ionization probability by assuming the *effective* path-length to be about $\frac{1}{3}d = 0.5\text{mm}$. Thus, after one day in helium, the ionization probability, $P_{1\text{ day}}$, is given by $P_{1\text{ day}} = 0.05\text{ cm}/430\text{ cm} \approx 1.2 \times 10^{-4} = 0.012\%$, while for 120 days $P_{120\text{ days}} = 0.05\text{ mm}/3.6\text{ cm} \approx 0.014 = 1.4\%$. In our simple model, we equate this ionization probability with the probability of after-pulsing.

4.4 Timing of after-pulses

As discussed above, the ionization of helium occurs when a photoelectron has sufficiently high energy, which for the M16 PMT occurs near the first dynode. The helium ion is then accelerated to the photocathode and may become the source of a secondary electron. Its travel time determines the time separation between the initial (helium ionizing) photoelectron and an electron ejected by an impact of a helium ion with the photocathode. This time can be roughly estimated by the time-of-flight of a helium ion along a straight line through the distance between the photocathode and the first dynode:

$$t = \sqrt{\frac{2d}{a}} = \sqrt{\frac{2dm_{He}}{\frac{\Delta V_1}{d}e}} = d\sqrt{\frac{2m_{He}}{\Delta V_1 e}} = 27\text{ ns},$$

where $d = 1.5\text{ mm}$, $\Delta V_1 = 135\text{ V}$, and a are a distance, voltage, and an acceleration of a helium ion between the photocathode and the first dynode, m_{He} is its mass, and e is a unit of an electric charge. In reality, the timing of helium ions will depend on the actual shape and strength of the electric field, and the place where the helium atom was ionized, so the time separation of the after-pulsing would be smeared around this average value.

5. Discussion

The presented estimate of the probability and timing of after-pulses roughly agrees with main features of the recorded data. The probability of after-pulsing increased with the exposure time to helium by about 1 to 4%, depending on the pixel. A significant fraction of after-pulses is attributed to the initial residual contamination of the M16 vacuum.

The time separation of observed after-pulses is consistent with the process of helium ionization by photoelectrons. The ionization can occur either between the first dynode and the photocathode or deeper in the dynode channel structure of the M16. Only after the photoelectrons gain sufficient energy and are close to the first dynode does the ionization cross-section become significant. In the M16 PMT this effectively reduces the mean-free-path for an electron to ionize helium atoms.

We believe that the observed resilience to helium permeation and the low probability of after-pulsing are due to the M16 compact dynode structure housed in a metal casing which operates at a negative potential of the photocathode. The electron energies achieved through the acceleration in the electric fields inside an M16 PMT are relatively small. This is because they depend on the voltage differences between dynodes which for the specific M16 voltage divider used by MINOS and the maximal operating HV of 1000V range from 56V to 135 V. Short distances that

electrons travel inside the tube and low voltage differences give the low probability of after-pulses as compared to larger photomultipliers with higher accelerating potentials, as for example studied in reference [18].

We studied after-pulses related only to dark noise single photoelectron pulses. Since signal light levels in MINOS are of the order of several to few tens of photoelectrons, our results are relevant to the MINOS detectors (although MINOS PMTs operated at a lower gain) but may not be for applications with significantly larger signals.

6. Conclusions

We have studied the effects of helium poisoning of R5900-00-M16 PMTs which were employed in the MINOS Far detector. A photomultiplier tube was immersed in pure helium atmosphere for about four months and its response was monitored using a digital oscilloscope. During this time, the PMT showed a slow increase in the probability of after-pulsing but its main performance characteristics degraded only slightly. The observed decrease of gain by a few percent is consistent with a typical aging of such PMTs [4].

In our tests, the primary pulses were caused by dark noise single photoelectrons. We observed that the probability of after-pulsing grew linearly with the PMT exposure time to helium, and that the primary pulses and the associated after-pulses have similar gains and widths. We conclude that our data indicate that this type of PMTs exhibits resilient response to helium poisoning.

We thank Yuji Yoshizawa and Wayne Stehle of Hamamatsu Photonics for providing PMTs for our tests and furnishing additional technical information and assistance. This work was supported in part by DOE grant DE-FG03-93ER40757.

References

- [1] P875: A Long-baseline Neutrino Oscillation Experiment at Fermilab, The MINOS Collaboration, Fermilab, February, 1995.
- [2] The MINOS Detectors, Technical Design Report, Fermilab, NuMI-L-337, Fermilab, October, 1998.
- [3] K. Lang [for MINOS Collaboration], Nucl. Instrum. Meth. A **461**, 290 (2001).
- [4] K. Lang *et al.*, Nucl. Instrum. Meth. A **545**, 852 (2005).
- [5] First beam paper: D. G. Michael *et al.* [MINOS Collaboration], Phys. Rev. Lett. **97**, 191801 (2006); the most recent paper: P. Adamson *et al.* [MINOS+ Collaboration], Phys. Rev. Lett. **122**, no. 9, 091803 (2019).
- [6] S. Avvakumov *et al.*, Nucl. Instrum. Meth. A **545**, 145 (2005).
- [7] The CDMS-II (Cryogenic Dark Matter Search) Experiment is located in the Soudan-2 cavern in the Soudan Underground Laboratory in Minnesota. The cavern is neighboring the new MINOS cavern also excavated 705m underground.
- [8] LabView is a product of National Instruments Corporation, 11500 N Mopac Expwy, Austin, TX 78759-3504, USA.
- [9] Private communication from Hamamatsu Photonics.

- [10] We used a digital oscilloscope model 584L made by LeCroy Corporation, 700 Chestnut Ridge Rd., Chestnut Ridge, NY 10977-6499, USA.
- [11] The thickness and exact composition of the photocathode constitutes proprietary information. We speculate that the photocathode is a bialkali layer of thickness of 2,000 to 10,000nm (i.e., a few hundred of atomic layers).
- [12] R. M. Barrer, *Diffusion in and through Solids*, Cambridge University Press, New York, 1941.
- [13] According to Hamamatsu Photonics, the composition of the M16 borosilicate glass front window is very close to Glass Designation 7056 with SiO_2 (68.0%), Al_2O_3 (3.0%), B_2O_3 (18.0%), LiO_2 (1.0%), Na_2O (1.0%), BaO (0.0%), K_2O (9.0%) which we used to find the value of the permeation constant K in reference [14].
- [14] J. E. Shelby, *Handbook of Gas Diffusion in Solids and Melts*, ASM International, Materials Park, OH, 1996 (ISBN: 0-87170-566-4);
- [15] V. O. Altemose, J. Appl. Phys. **32**(7), 1309 (1961).
- [16] M. B. Shah, D. S. Elliot, P. McCallion and H. B. Gilbody, J. Phys. B. At. Mol. Opt. Phys. **21**, 2751 (1988).
- [17] R. G. Montague, M. F. A. Harrison and A. C. H. Smith, J. Phys. B. At. Mol. Opt. Phys. **17**, 3295 (1984).
- [18] J. R. Incandela *et al.*, Nucl. Instrum. Meth. **A269**, 237 (1988).